The Astrophysical Journal, 717:458–467, 2010 July 1 doi:10.1088/0004-637X/717/1/458

SPATIAL SEISMOLOGY OF A LARGE CORONAL LOOP ARCADE FROM *TRACE* AND EIT OBSERVATIONS OF ITS TRANSVERSE OSCILLATIONS

E. Verwichte, C. Foullon, and T. Van Doorsselaere
Centre for Fusion, Space and Astrophysics, Department of Physics, University of Warwick, Coventry CV4 7AL, UK; Erwin.Verwichte@warwick.ac.uk
Received 2010 March 17; accepted 2010 May 5; published 2010 June 14

ABSTRACT

We present a study of transverse loop oscillations in a large coronal loop arcade, using observations from the *Transition Region And Coronal Explorer* (*TRACE*) and Extreme-ultraviolet Imaging Telescope (EIT). For the first time we reveal the presence of long-period transverse oscillations with periods between 24 minutes and 3 hr. One loop bundle, 690 Mm long and with an oscillation period of 40 minutes, is analyzed in detail and its oscillation characteristics are determined in an automated manner. The oscillation quality factor is similar to what has been found earlier for oscillations in much shorter loops. This indicates that the damping mechanism of transverse loop oscillations is independent of loop length or period. The displacement profile along the whole length of the oscillating loop is determined for the first time and consistently between *TRACE* and EIT. By comparing the observed profile with models of the three-dimensional geometry of the equilibrium and perturbed loop, we test the effect of longitudinal structuring (spatial seismology) and find that the observations cannot unambiguously distinguish between structuring and non-planarity of the equilibrium loop. Associated intensity variations with a similar periodicity are explained in terms of variations in the line-of-sight column depth. Also, we report intensity oscillations at the loop footpoint, which are in anti-phase with respect to the intensity oscillations in the loop body. Lastly, this observation offers the first opportunity to use the transverse oscillations of the arcade to model the Alfvén speed profile in the global corona.

Key words: magnetic fields – magnetohydrodynamics (MHD) – Sun: corona – Sun: oscillations

Online-only material: color figures

1. INTRODUCTION

Transverse waves and oscillations are observed in solar coronal structures in connection with eruptions (e.g., Aschwanden et al. 1999a; Nakariakov et al. 1999; Verwichte et al. 2005). The majority of the observational studies have been made with the *Transition Region And Coronal Explorer* (*TRACE*), although observations using the *Solar TErrestrial RElations Observatory* (*STEREO*; Verwichte et al. 2009), *Hinode* (Van Doorsselaere et al. 2008b), and from ground-based observatories exist as well (Hori et al. 2005; Tomczyk et al. 2007). Transverse loop oscillations are standing modes that manifest themselves by periodic displacements of the loop axis. They have been interpreted as a magnetohydrodynamic kink mode (Aschwanden et al. 1999a; Nakariakov et al. 1999). This mode is quasi-incompressible and represents the equivalent of the shear Alfvén wave for a structured plasma (Van Doorsselaere et al. 2008a; Goossens et al. 2009). The typically observed period of transverse loop oscillations is 5 minutes. There are only a few cases where periods about and above 10 minutes have been reported, which may be associated with such oscillations in loops (Aschwanden et al. 2002; Foullon et al. 2005; Hori et al. 2005; Verwichte et al. 2009). Because of the restricted field of view of the *TRACE* instrument, there is an instrumental bias against detecting long-period transverse loop oscillations. Therefore, larger loops, which potentially support long-period oscillations, are not fully observed by *TRACE*. On the other hand, instruments with larger fields of view, such as the Extreme-ultraviolet Imaging Telescope (EIT) on board the *Solar and Heliospheric Observatory* (*SOHO*) and the Extreme Ultraviolet Imager (EUVI) on board *STEREO*, have worse spatial resolution than *TRACE* and can only detect the largest loop displacements. Transverse loop oscillations damp quickly within several oscillation periods, for which various theories have been developed, i.e., resonant mode conversion (e.g., Ruderman & Roberts 2002; Arregui et al. 2008), wave leakage (Brady & Arber 2005; Mikhalyaev & Solov'ev 2005; Brady et al. 2006; Verwichte et al. 2006b; Terradas et al. 2006), loop cooling (Morton & Erdélyi 2009), and phase mixing (Ofman & Aschwanden 2002; Luna et al. 2008).

The report of multiple simultaneous oscillation harmonics within the same loop (Verwichte et al. 2004) has triggered much theoretical work on the effect of longitudinal structuring, i.e., density stratification and magnetic field expansion. An extensive review on the topic can be found in Andries et al. (2010). First, the relation between the oscillation periods of harmonics has been exploited (Andries et al. 2005). Unfortunately, there exist only few observational examples (Verwichte et al. 2004; Van Doorsselaere et al. 2007, 2009; De Moortel & Brady 2007) with multiple modes simultaneously detected. Second, in a method dubbed "spatial seismology," the theory of the modification of the spatial structure of the oscillation eigenfunctions due to longitudinal structuring has been investigated (e.g., Erdélyi & Verth 2007; Verth & Erdélyi 2008; Andries et al. 2009). However, the application of this method to observations may be challenging due to the difficulties in obtaining accurately the loop geometry, projected displacement profile, and mode polarization. Thus far, only one study exists of a transverse loop oscillation observed with *STEREO* for which the three-dimensional structure and polarization has been obtained (Verwichte et al. 2009). Unfortunately, in that case it was difficult to measure the projected displacement profile along the whole loop due to line of sight confusion. Here, we shall study in detail an observation of a long-period, large amplitude transverse oscillation in a large-scale coronal loop arcade. This event provides a unique opportunity to characterize the oscillation displacement profile and explore the applicability of spatial seismology.

The basic theory of transverse loop oscillations in terms of kink modes predicts no significant density variations because of the near-incompressibility of the mode. However, there are several mechanisms through which intensity variations may be associated with transverse loop oscillations. First, the displacements of the loop may lead to variations in the line-of-sight column depth. Hence, even though the density remains constant, the integrated intensity varies with time (Cooper et al. 2003). Verwichte et al. (2009) showed that this effect is responsible for the observed intensity variations in an oscillation seen by *STEREO*. Katsiyannis et al. (2003) and O'Shea et al. (2007) have also interpreted, using this mechanism, and observed intensity oscillations as transverse waves. However, in those studies, conclusive measurements of the transverse displacement oscillation of the loop were not available. In a second mechanism, according to an extension of the basic model to include curvature, density variations are expected for the vertically polarized mode as the loop length or cross section varies (Verwichte et al. 2006a). This effect was reported by Wang & Solanki (2004) using *TRACE* observations. A third mechanism is nonlinear coupling through the ponderomotive force of the kink mode to a slow magnetoacoustic mode (e.g., Verwichte et al. 1999). Terradas & Ofman (2004) studied intensity variations of transverse loop oscillations arising from the ponderomotive force. Such variations manifest themselves on a slower acoustic time scale than the observed transverse oscillations. Alternatively, a transverse loop oscillation may be interpreted as arising from the nonlinear centrifugal force associated with a slow magnetoacoustic mode. The loop intensity would then oscillate at an acoustic time scale with a period double that of the loop displacement.

Section 2 introduces the *TRACE* and EIT observations and the oscillating loop event. In Section 3, the transverse loop oscillations are examined in detail and the oscillation parameters are determined. In Section 4, the spatial displacement profile of one particular loop is studied. In Section 5, the intensity variations associated with the transverse loop oscillation are presented. In Section 6, the implications of this study for the measurement of the Alfvén speed profile in the global corona are discussed. Finally, in Section 7, the main findings are summarized and discussed.

2. OBSERVATIONS

We study the active region NOAA 09608 on 2001 September 15 between 09:00 and 17:00 UT using the EIT (Delaboudinière et al. 1995) and *TRACE* instruments (Handy et al. 1999). EIT full disk images are taken every 12 minutes as part of the synoptic coronal mass ejection (CME) watch program, in the 195 Å bandpass, which is sensitive to 1.6 MK plasma. The EIT CCD image pixel size is 2.″59. Figure 1 shows the southwest quadrant of an EIT image, where the active region is located with a large loop arcade visible above the limb (see also Figure 2). During this period, *TRACE* took images of the north part of the active region approximately every 35 s in the 171 Å bandpass, which is sensitive to coronal plasmas with temperatures around 1 MK. The *TRACE* CCD image pixel size is 0.″5. Figure 1 shows the southmost part of the *TRACE* field of view that has been used in this study.

Around 11:04 UT, an M1.5 *GOES* level flare and associated CME occur in the active region. In the EIT images, the eruption seems to push downward the lower part of the arcade (roughly 0.5 solar radii above the surface), whilst pushing the higher part upward. Following the impulse, the arcade loops are seen over

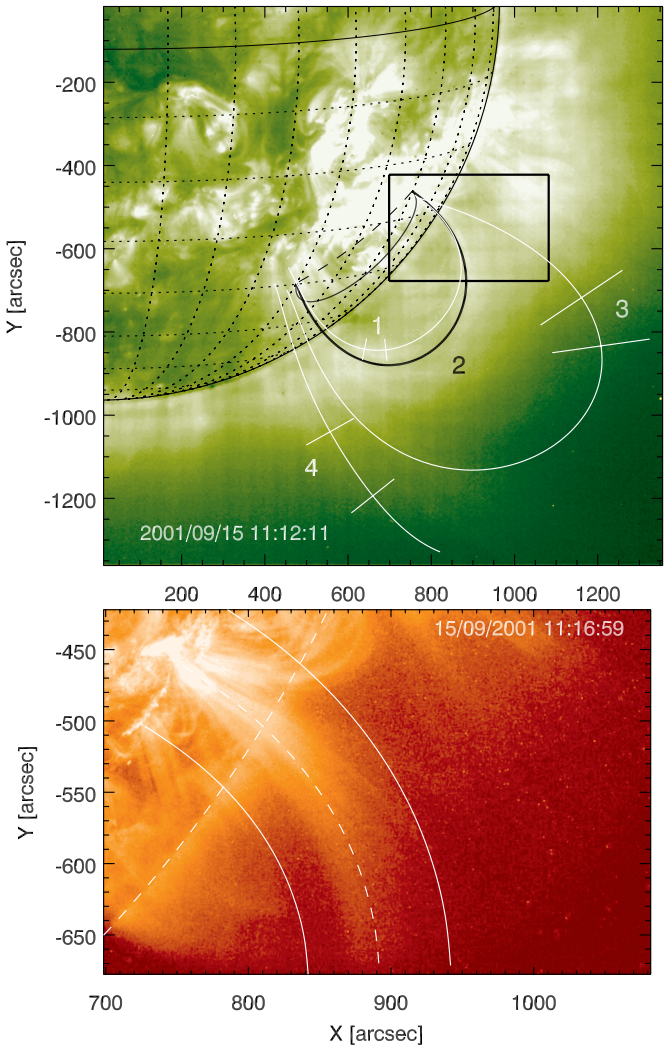

Figure 1. Top: southwest quadrant of an EIT image taken at 11:12:11 UT on 2001 September 15, showing active region NOAA 09608 near the west limb at (700″, −497″) from disk center. The used *TRACE* field of view is shown as a black rectangular box. The paths of four loops are indicated. Loop no. 2 (black line) is studied in more detail and the projection of the loop onto the solar surface is shown as well, based on the planar loop geometry model that minimizes curvature (see details in the text). In the other three loops, white tick marks indicate the intervals where the loop oscillation is investigated. Bottom: *TRACE* field of view of the northern leg of the active region loop arcade at 11:17 UT on 2001 September 15. The parallel dashed and solid curves show the central path and width of the loop data cut used, respectively.

(A color version of this figure is available in the online journal.)

a time range of an hour to oscillate transversely with periods in the range of 20–60 minutes. Figure 2 shows a sequence of EIT difference images in which the whole loop arcade is seen to oscillate. However, the oscillations are not resolved well in time. *TRACE* observed only the northern leg of the loop arcade. Because the displacement amplitude is so large, it is still possible to resolve the displacement oscillation far from the loop top. In principle, information of the mode polarization can be obtained from the difference images (Wang et al. 2008). However, in this instance, this is difficult because the scene is confused by the oscillation of multiple nearby loops with different periods. Nevertheless, as we shall see later, the observation is consistent with a horizontally polarized mode, which would be excited by the CME erupting from the heart of the active region pushing the loop arcades sideways. Such long periods in transverse

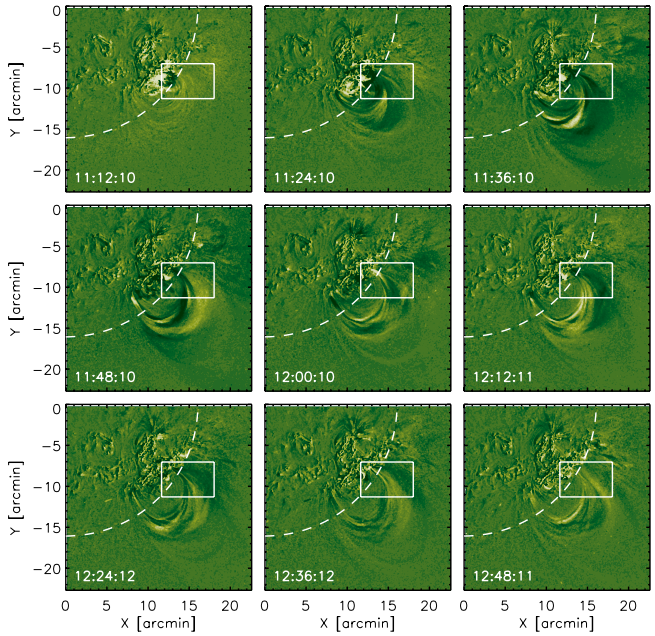

Figure 2. Sequence of EIT difference images, where at each time the image has been subtracted by the previous image taken 12 minutes earlier. The solar limb (dashed line) and the used *TRACE* field of view (rectangular box) are indicated.

(A color version of this figure is available in the online journal.)

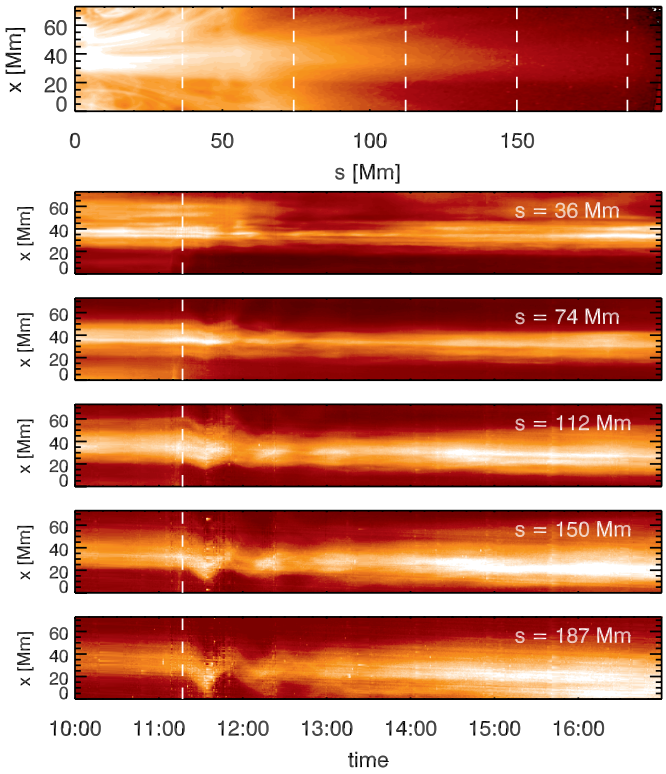

Figure 3. *TRACE* loop path image as a function of loop distance s and transverse coordinate x, showing the average intensity between 10:00 and 10:16 UT. $x = 0$ corresponds to the sunward side of the loop path. The five vertical dashed lines are transverse cuts that are shown as a function of time below. The vertical dashed line in each time-space plots is the reference time t_0.

(A color version of this figure is available in the online journal.)

loop oscillations have not been reported before. The transverse displacements in the plane of the sky are in the order of tens of megameters. Therefore, exceptionally, EIT can detect these oscillations. The paths of four loops are indicated in Figure 1. Within the *TRACE* field of view, the leg of a loop bundle that is part of the arcade corresponds to loop no. 2. We shall examine the oscillations of this bundle in detail.

The three-dimensional geometry of the loop bundle 2 is modeled by adding to the plane of sky projected loop path a depth coordinate that ensures that the whole loop lies within a plane. Because the loop is observed from one viewpoint only, the inclination of that plane with respect to the photospheric normal is a free parameter. The details of the method are outlined in the Appendix. Similarly to Aschwanden (2010), we choose the inclination that minimizes variations of the loop curvature. Thus, a loop is found with a length of 690 Mm, height above the surface of 190 Mm, and inclination from the surface normal of 43° southward. The loop footpoints are separated by 22° (271 Mm). The photospheric normal at the center of the loop baseline makes an angle with the line of sight of 60°. The loop plane makes an angle of −13° with respect to the plane of the sky. Within the loop plane, the loop shape can be approximated by a circle with a radius of 161 Mm and the origin at a distance of 75 Mm above the photospheric point halfway between the two footpoints. From the *TRACE* observation (Figure 1), the square root of the intensity is measured along the loop bundle and has a best fit with a damped exponential with a scale height of 85 Mm. The loop covers two density scale heights.

In order to verify this specific loop geometry, we employ the method of dynamic stereoscopy (Aschwanden et al. 1999b), which makes use of solar rotation to create two view points of the same loop from images taken at two different times. We have rotated the three-dimensional loop to an earlier date (one day before) and compared with an EIT image of that date. Because of diffuseness of the loop arcade in the EIT image, it is not possible to apply this method rigorously because of the difficulty of clear identification of the same loop at both dates. Nonetheless, it shows that our choice of loop geometry is reasonable within a plausible range from 30° to 60° south. In this range, the loop length would vary between 678 and 751 Mm. This uncertainty would introduce an error in the loop length of only 9%.

A two-dimensional data cut is interpolated from the *TRACE* data set along the path of the loop bundle with a width of 100″ or 73 Mm (see Figures 1 and 3). The geometrical loop model is used to ensure the path follows the loop bundle as it moves due to solar rotation. Also, the model provides a coordinate s from the footpoint along the loop, which reaches a distance of approximately 199 Mm in the *TRACE* field of view, which is 29% of the loop length. Figure 3 shows time-space plots from the loop data at various distances along the loop bundle. The transverse loop oscillation is visible between 11:00 and 14:00 UT as a sequence of 2–3 transverse displacements of the loop axis. The oscillation starts with a (projected) downward displacement of the loop. Also, the increase of the displacement amplitude as a function of loop distance s is apparent.

3. ANALYSIS OF THE OSCILLATION

The relevant parameters describing the transverse loop oscillation are determined automatically from the *TRACE* data in the following manner. Figure 4 shows an example of the automated procedure. At each value of s, we have a transverse profile of intensity, $I_s(x, t)$, as a function of the transverse coordinate and time. The intensity profile $I_s(x)$ at time t is correlated with the intensity profile $I_s(x, t_0)$ at reference time $t_0 = 11{:}16{:}59$ UT for a lag in x that maximizes the correlation. In this fashion, an

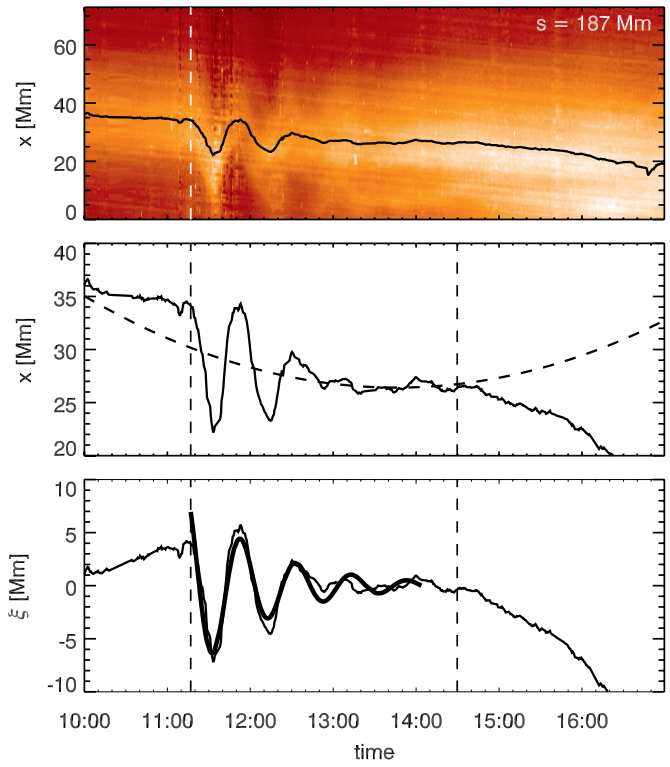

Figure 4. Top: transverse cut at $s = 187$ Mm showing the loop intensity as a function of time and transverse coordinate, x. The automatically determined time series of the transverse location loop axis is shown. Middle: transverse location loop axis as a function of time. The dashed line is a quadratic trend fitted to the time series in the time range indicated by the two vertical dashed lines. Bottom: the loop displacement time series, $\xi(t)$, as a function of time. The thick curve is the fitted damped oscillation.

(A color version of this figure is available in the online journal.)

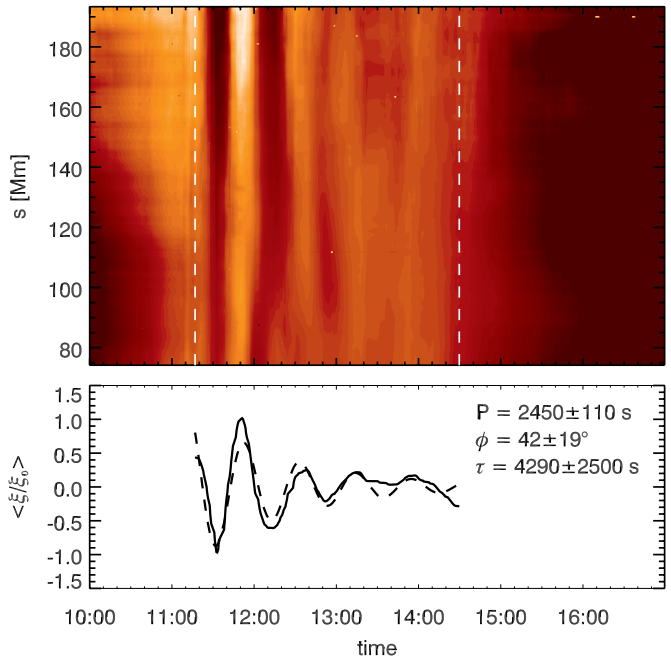

Figure 5. Top: displacement time series as a function of time and loop location s. Bottom: displacement time series normalized by displacement amplitude and averaged over s, $\langle \xi/\xi_0 \rangle$, as a function of time. The thick curve is a fitted damped oscillator with the given parameters.

(A color version of this figure is available in the online journal.)

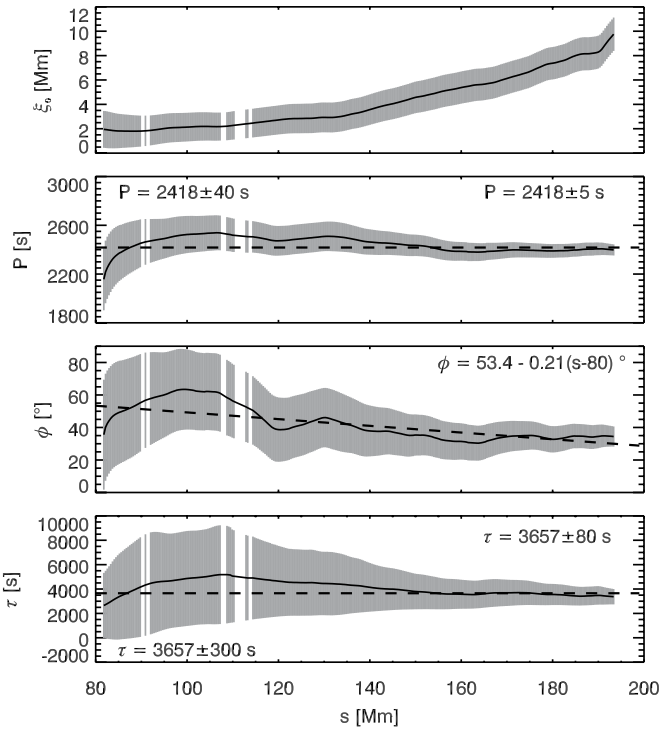

Figure 6. Oscillation displacement amplitude ξ_0, period P, phase ϕ, and damping time τ as a function of loop location s. Dashed lines are averages or lines fitted over the whole interval and quantified on the left.

approximate transverse location of the loop axis as a function of time is determined. This is used as the initial guess for a fit of the intensity profile $I_s(x)$ with a Gaussian profile on top of a quadratic background. The location of the maximum of the fitted Gaussian is taken as the location of the loop axis. Between times t_0 and $t_1 = 14{:}30$ UT, a quadratic trend is fitted to the location time series. The time series that emerges from subtracting this trend from the loop location is the loop displacement time series, $\xi(t)$. This transverse displacement represents the projected displacement of the loop axis in the plane of the sky in the direction perpendicular to the unperturbed loop axis.

This time series is fitted within the time interval $[t_0,t_1]$ by a damped oscillation of the form $\xi(t) = \xi_0 \exp(-(t - t_0)/\tau) \cos(2\pi(t - t_0)/P + \phi)$, where the fitting parameters ξ_0, P, τ, and ϕ are the displacement amplitude, oscillation period, e-folding damping time, and phase, respectively. As an error on the displacement time series, a constant value of ten *TRACE* pixels has been assumed. In this manner, the oscillation parameters are determined reliably at 282 out of 317 locations in s between 74 and 193 Mm. The small subset of 35 locations where the fit failed has been ignored rather than re-examined in more detail. The time series show no evidence of the presence of multiple oscillation periods due to higher harmonics. Figure 5 shows the displacement time series, $\xi(t)$, at all used values of s. It shows a spatially coherent consistent oscillatory pattern across all values of s. The amplitude of the oscillation can be seen to steadily increase with s. After dividing each time series by the amplitude ξ_0, which increases from 2 to 10 Mm over the interval, we can combine all time series and find an average time series $\langle \xi/\xi_0 \rangle$, which shows the oscillation clearly.

Figure 6 shows the oscillation parameters as a function of distance, s, along the loop bundle. P and τ do not vary greatly along the loop. We can calculate the error on P and τ averaged over the interval in two manners. First, following Verwichte

Table 1
Approximate Loop and Oscillation Parameters for Three Additional Loops, Together with the Equivalent Parameters for the Detailed Studied Loop Bundle, 2

Loop No.	L (Mm)	P (s)	$V_{\rm ph}$ (km s^{-1})
1	$\gtrsim$610	1440 ± 230	$\gtrsim$850
2	680	2418 ± 5	562
3	$\gtrsim$1280	4900 ± 900	$\gtrsim$520
4	(2000–3000)	(10800)	(460)

Note. Values within brackets have large uncertainties.

et al. (2004) we take the standard deviation of this spread as a measure of the error on the parameter. Thus, we find $P = 2420 \pm 40$ s and $\tau = 3660 \pm 300$ s. This corresponds to a period and damping time of 40.3 ± 0.7 minutes and 61 ± 5 minutes, respectively. Second, we can improve the error on those parameters by considering the measurements at each s to be independent samples of the one true value and calculate the error as $\sigma^2 = (\sum_s 1/\sigma_s^2)^{-1}$, where σ_s is the error at each s (Van Doorsselaere et al. 2007). Thus, we find $P = 2418 \pm 5$ s and $\tau = 3660 \pm 80$ s. This corresponds to $P = 40.3 \pm 0.8$ minutes and $\tau = 61 \pm 1$ minutes. This is the first time a transverse loop oscillation with an oscillation period over 20 minutes has been reported. We can describe the phase with a linear fit of the form $\phi(s) = 53.^{\circ}4 - 0.21 \times (s - 80)^{\circ}$. Over the interval, the phase has an average of 42°.

The oscillation quality factor is $\tau/P = 1.48 \pm 0.03$, where we have used the second error estimation. Furthermore, the oscillation phase speed is $V_{\rm ph} = 2L/P = 580 \pm 50$ km s^{-1}. For the fundamental kink mode in a thin loop and in the zero plasma-β limit, $V_{\rm ph}$ is equal to the kink speed, $C_{\rm K}$, which is given by $C_{\rm K}^2 = 2V_{\rm A}^2/(1 + \rho_{0e}/\rho_{0i})$ (Edwin & Roberts 1983). Here, $V_{\rm A}$ is the loop Alfvén speed and ρ_{0e}/ρ_{0i} is the loop density contrast, calculated as the ratio of the external and internal mass densities. From the kink speed a minimum average loop Alfvén speed can be derived under the assumption of large loop density contrast as $V_{\rm ph}/\sqrt{2} \leqslant V_{\rm A} \leqslant V_{\rm ph}$ (Nakariakov & Ofman 2001). Thus, we find $V_{\rm A} \geqslant 410 \pm 40$ km s^{-1}.

Besides the loop bundle that has been analyzed in depth, there are other loops in the same arcade that show oscillations. However, these loops are not visible with *TRACE*. We make an estimate of the oscillation period in three further loops using EIT (shown in Figure 1). Table 1 shows the estimated oscillation periods and loop lengths, where we have assumed for simplicity that the loops have a similar inclination as the previously studied loop. Then the loop planes lie approximately in the plane of the sky, and the projected loop length is close to the real length. We find oscillation periods as long as 3 hr. The phase speeds of loops 2, 3, and 4 are similar, around 500 km s^{-1} (bearing in mind that the loop length estimates are approximate).

4. SPATIAL PROFILE OF THE TRANSVERSE OSCILLATION

The projected transverse displacement amplitude, ξ_0, measured by *TRACE* in the northern loop leg, increases with height and reaches 10 Mm. It is expected that this amplitude increases further toward the top of the loop bundle. Therefore, we use EIT to characterize the transverse displacement amplitude over the whole loop bundle. We measure the loop location at time 11:36:10 UT, near the time when the loop is displaced the most, and compare it with its location at 11:12:10 UT when the loop is

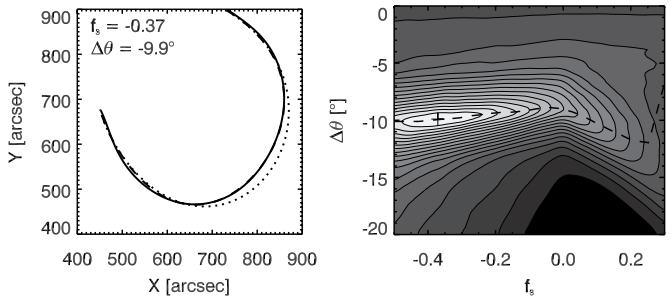

Figure 7. Left: loop path in plane of sky at times 11:12:10 (dotted line) and 11:36:10 UT (solid line). The dashed line is the loop perturbed with a displacement of the form given by Equation (2) with $f_3 = -0.37$. The dotted curve is the equilibrium loop. Right: parameter space f_3-$\Delta\theta$ showing the measure of agreement between the model and observed perturbed loop. The maximum value is indicated by a cross. The dashed line follows the path of maximum overlap as a function of f_3.

unperturbed. The two loop paths are shown in Figure 7. Figure 8 shows ξ_0 as a function of distance along the loop. The measurement from EIT is consistent with the more accurate *TRACE* measurements discussed in the previous section.

The curve is not expected to resemble a simple sinusoidal shape because of perspective effects, i.e., the loop plane does not lie in the plane of the sky. To model this profile, from the unperturbed loop geometry the perturbation for a horizontally polarized mode is constructed by inclining the loop plane by a constant angle $\Delta\theta = -10^{\circ}$. This is shown as the long dashed curve in Figure 8(a). Overall, this matches the observation pretty well, which confirms that the mode is horizontally polarized. However, between $s/L = 0.05$ and 0.35 the model overestimates the measured displacement. Can this be modeled more accurately?

Various studies show that longitudinal structuring leads the loop displacement profile to depart from a simple sinusoidal shape (e.g., Erdélyi & Verth 2007; Verth & Erdélyi 2008). In particular, Andries et al. (2009) showed that the displacement profile, besides the usual contribution of the form $\sin(\pi s/L)$, has contributions from higher odd sinusoidal harmonics. Therefore, the easiest manner in which to extend our displacement model is to include a third longitudinal harmonic of the form $\sin(3\pi s/L)$ with an amplitude f_3 relative to the fundamental mode, i.e.,

$$\xi_0(s) = \xi_{0\rm M} \frac{\left[\sin\left(\frac{\pi s}{L}\right) + f_3 \sin\left(\frac{3\pi s}{L}\right)\right]}{1 + |f_3|} . \quad (1)$$

The displacement amplitude $\xi_{0\rm M}$ is associated with an angle $\Delta\theta = \xi_{0\rm M}/\max(h)$, where $h(s)$ is the distance between an unperturbed loop location and its footpoint baseline. The total angle at which the loop plane is inclined is the sum of the unperturbed loop inclination, θ_0 and the perturbation angle ξ_0/h:

$$\theta(s) = \theta_0 + \frac{\xi_0(s)}{h(s)} = \theta_0 + \Delta\theta \frac{\max(h)}{h} \frac{\left[\sin\left(\frac{\pi s}{L}\right) + f_3 \sin\left(\frac{3\pi s}{L}\right)\right]}{1 + |f_3|} . \quad (2)$$

For a semi-circular loop with $h(s)/\max(h) = \sin(\pi s/L)$, and $f_3 = 0$, the simple case of a constant inclination of the loop plane is recovered, i.e., $\theta = \theta_0 + \Delta\theta$. However, for the general case of a non semi-circular loop, the perturbed loop will no longer be planar. Also, note that the case $f_3 = 0$ does not correspond to a constant inclination because the loop studied

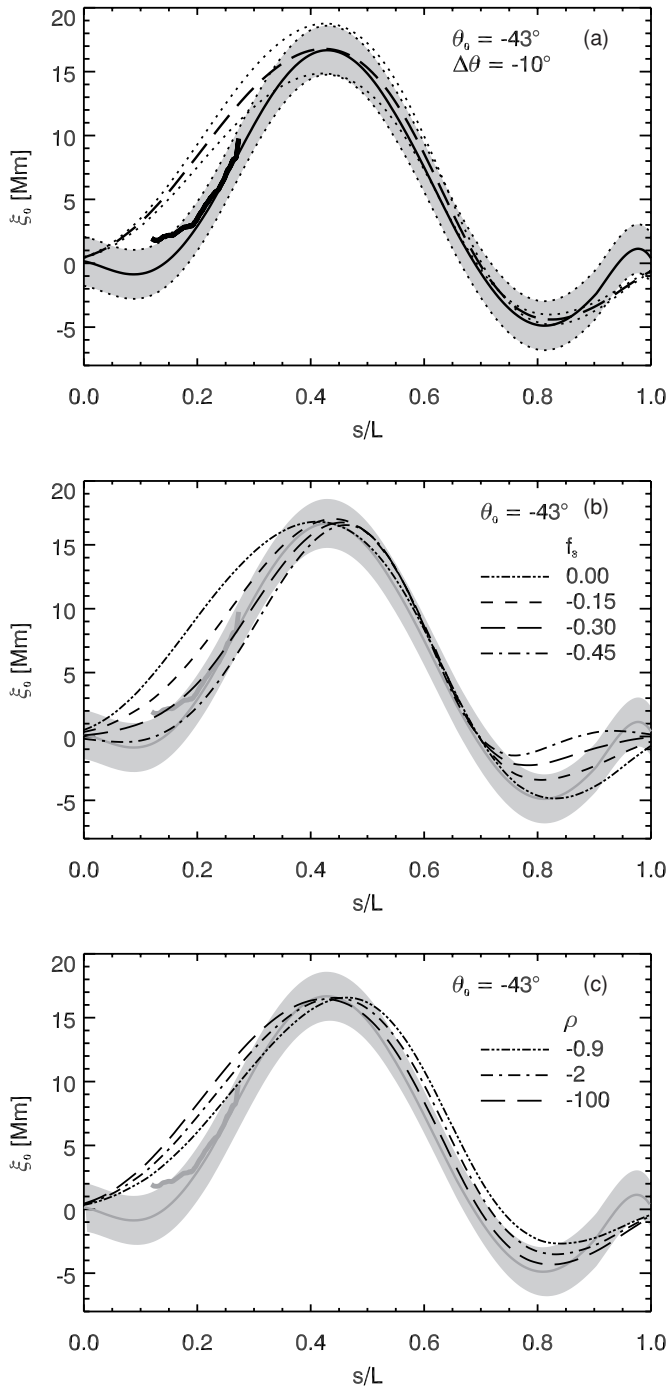

Figure 8. Transverse displacement amplitude, ξ_0, as a function of distance along the loop, s/L. The solid line is the measurement using EIT. The gray area indicates an error of one EIT pixel either side of the curve. The thick solid line is the measurements using *TRACE*. (a) The long dashed line is the (projected) displacement amplitude for a horizontally polarized fundamental mode which is constructed by inclining the unperturbed loop by a constant angle of $\Delta\theta = -10^\circ$. The dotted lines either side of this curve represent the solutions for $\Delta\theta = -9^\circ$ (lower curve) and $\Delta\theta = -11^\circ$ (upper curve). (b) Value of f_3 in a model that optimally fits the observed loop displacement, as a function of loop inclination θ_0. The value of $\theta_0 = -43^\circ$ is indicated by a vertical dashed line. (c) Curves using a non-planar loop for three values of ρ are shown.

here is not semi-circular. Figure 8(b) shows the projected loop displacement based on Equation (2) for four values of f_3. Indeed, by decreasing f_3, the difference between model and observation in the interval $s/L = 0.05$–0.35 is eliminated. Figure 7 shows the measure of agreement between the observed perturbed loop and the model as a function of f_3 and $\Delta\theta$. The best fit occurs for $f_3 = -0.37$ and $\Delta\theta = -9.^\circ9$. This corresponds to a maximum displacement of the loop top of $\xi_0 = 41$ Mm. The perturbed loop shape associated with these values is shown in Figure 9.

A remaining question for this model concerns the sensitivity of f_3 to the choice of unperturbed loop inclination θ_0. At each value of θ_0, we find the optimal value of f_3 by varying $\Delta\theta$. Figure 10 shows the dependence of f_3 on θ_0. For $\theta_0 > -43^\circ$, the dependency is strong and quickly goes to values of $|f_3|$ larger than unity. This is unrealistic as it would imply, contrary to the observations, that the oscillation is predominantly a third longitudinal harmonic. For $\theta_0 < -43^\circ$, the profile flattens with f_3 between -0.3 and -0.15. Of course, the more the loop is assumed to be inclined southward, the larger is the displacement needed to match the observations. For $\theta_0 = -60^\circ$, unrealistically large values of $\Delta\theta = -27^\circ$ and $\xi_0 = 103$ Mm are required and the loop would touch the solar surface.

It has to be borne in mind that the unperturbed loop has been assumed to be planar. One possibility remains that the difference between model and observation is explained by perturbing a non-planar loop by a constant inclination angle, $\Delta\theta$. To explore the non-planar loop geometry, we consider that the loop lies on the surface of a cylinder of radius ρ with the loop baseline parallel to the cylinder axis; the location of the baseline on the cylinder surface is determined by the equilibrium inclination θ_0 (see the Appendix). Thus, this model involves two free parameters, θ_0 and ρ. For simplicity we fix θ_0 to the previously found inclination. We allow ρ to vary. For $\rho \to \infty$ a planar loop is recovered. Also, ρ cannot be arbitrarily small because the cylinder has to be large enough to cover the loop in the plane of the sky. Figure 8(c) shows the projected loop displacement with a constant perturbed inclination $\Delta\theta$ for various values of ρ. This example illustrates that, in comparison with a planar loop perturbed with a constant inclination, it is possible to improve the match with the observation by making the loop non-planar. Therefore, the mismatch between model and observation does not need to be fully explained by a modified perturbation profile as Equation (2). In conclusion, from the observation, details of the loop displacement profile can be deduced, provided assumptions about the loop geometry are made, i.e., inclination, non-planarity.

5. INTENSITY OSCILLATIONS

Importantly, together with the transverse loop displacements, intensity variations are also seen. The time-space plots in Figure 3 show intensity enhancements that coincide with projected downward loop displacements. Figure 11 shows the relative intensity as a function of time and distance along the loop, averaged over the transverse coordinate. At distances above, say 70 Mm, the intensity enhancements are visible as an oscillatory pattern in relative intensity. The amplitude is of the order of 10% of the background intensity. This oscillation is characterized with a period $P = 2670 \pm 150$ s $= 44.5 \pm 2.5$ minutes and damping time $\tau = 3260 \pm 1400$ s $= 54.3 \pm 23.3$ minutes. These values roughly correspond to those found for the transverse displacement oscillation. The phase of the oscillation (relative to t_0) is $\phi = 183 \pm 33^\circ$.

Figure 11 also shows an oscillatory pattern near the footpoints, which appear to be in anti-phase with respect to the oscillations in the loop leg. At 11:50 UT, there is also a hint of downward propagation of the intensity phase at a speed of roughly 100 km s^{-1}. We investigate the footpoint intensity

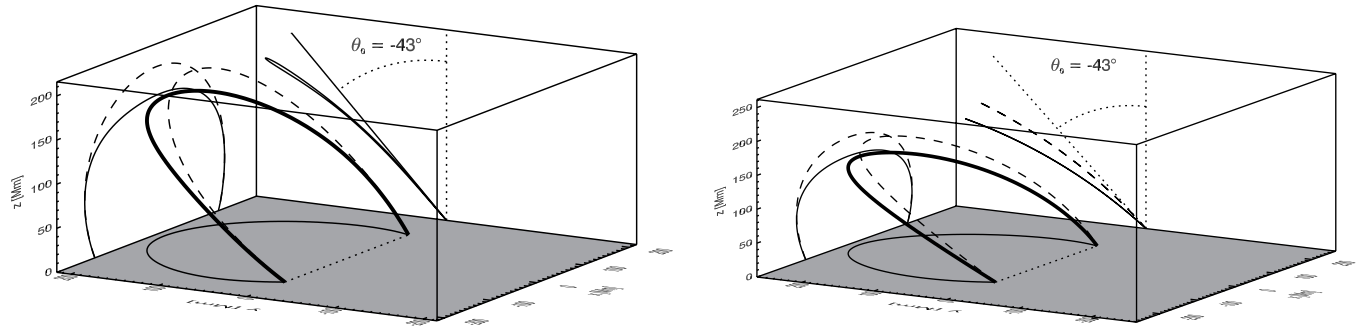

Figure 9. Three-dimensional shape of the perturbed (solid) and unperturbed (dashed) loops in a local coordinate system. Projections of the loops in two directions are also shown. Left: planar equilibrium loop perturbed by a displacement given by Equation (2) with $f_3 = -0.37$ and $\Delta\theta = -10°$. Right: non-planar equilibrium loop perturbed with by a displacement corresponding to a constant inclination angle with $\rho = -0.9$ and $\Delta\theta = -10°$.

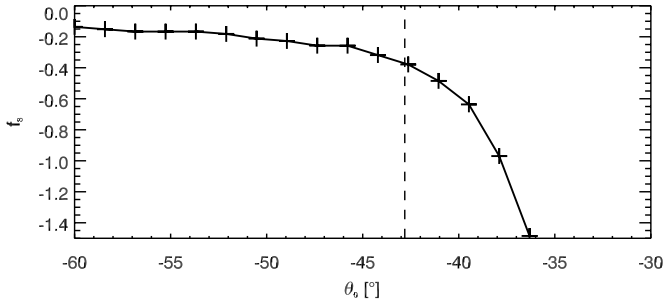

Figure 10. Value of f_3 in a model that optimally fits the observed loop displacement, as a function of loop inclination θ_0. The value of $\theta_0 = -43°$ is indicated by a vertical dashed line.

oscillation in more detail. Figure 12 shows the relative intensity as a function of time near the footpoint (averaged over the interval between $s = 0$ and $s = 22$ Mm). The oscillatory pattern is visible with a period $P = 2860 \pm 1000$ s $= 47.7 \pm 17$ minutes and damping time $\tau = 5190 \pm 2150$ s $= 86.5 \pm 36$ minutes that approximately match the characteristics found for the transverse displacement oscillation. The phase, $\phi = 19° \pm 20°$, is approximately in anti-phase with the intensity oscillation higher up in the loop. Furthermore, Figure 2 seems to suggest that the intensities at the two footpoints are oscillating in anti-phase with respect to each other (comparing times 11:48, 12:00, and 12:12 UT).

Since the oscillation periods are similar, nonlinear mechanisms, such as the ponderomotive excitation of a second harmonic slow mode or the centrifugal generation of transverse motions from a slow mode, are excluded. In Verwichte et al. (2009), intensity variations were found associated with a transverse loop oscillation and interpreted as variations in the line-of-sight column depth due to variations in the loop inclination. Figure 13 shows the principle in a simplified geometry where the line of sight is perpendicular to the photospheric normal and the loop baseline. The intensity from a loop segment can be described as $I = \epsilon 2a/\cos\theta$, where ϵ is the emissivity, $2a$ is the loop width, and θ is the loop inclination with respect to the observer. This means that the loop intensity I increases as the loop inclines away from the normal, independently of whether the inclination is toward or away from the observer. We can distinguish two cases. First, if $\Delta\theta > |\theta_0|$, the loop will be inclined toward and away from the observer during its oscillation. The resulting oscillation in intensity may have double the period of the transverse motion. Second, if $\Delta\theta < |\theta_0|$, the loop will always be either inclined toward or away from the observer (as shown in Figure 13). For this case, the intensity oscillation will

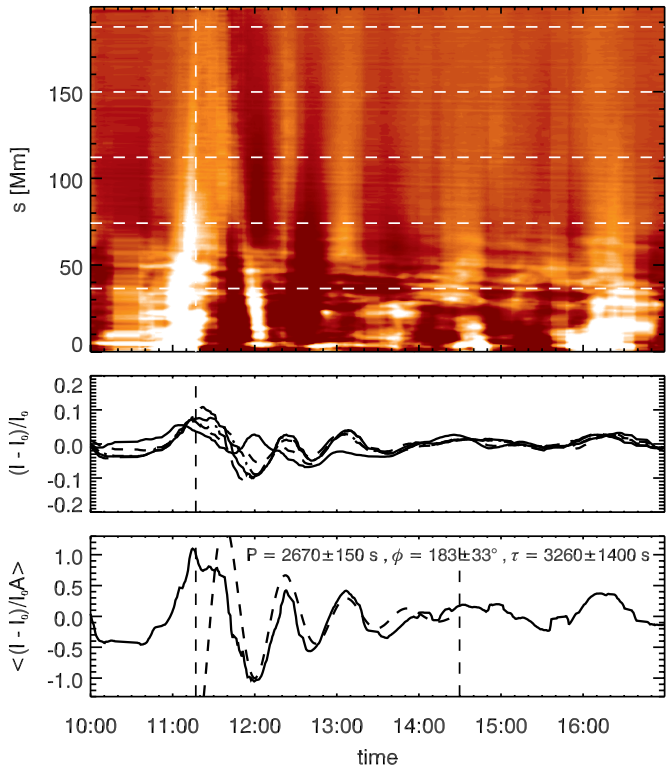

Figure 11. Top: relative intensity of the *TRACE* two-dimensional loop region, averaged over the transverse coordinate, as a function of time and distance along the loop bundle. Horizontal dashed lines indicate the locations from which the curves shown in the middle plot. The vertical dashed line indicates the reference time t_0. Middle: relative intensity at various distances along the loop, indicated by the horizontal dashed line in the top figure at $s = 36$ (solid), 74 (dashed), 112 (dot-dashed), 150 (triple dot-dashed), and 187 (long dashed) Mm. Bottom: relative intensity, normalized by the relative intensity amplitude profile $A(s)$, averaged over the interval in s between 74 and 193 Mm. A damped oscillator, fitted to the curve between times t_0 and t_1, is shown as a dashed curve.

(A color version of this figure is available in the online journal.)

have the same period as the transverse motion. We estimate the amplitude of intensity variations as the difference between the perturbed loop inclined by a further $\Delta\theta$ and the unperturbed loop, i.e., $\Delta I/I_0 = \cos\theta_0/\cos(\theta_0 \pm \Delta\theta)$. We have to take into account the angle between the photospheric normal of the loop baseline and the line of sight. Thus, $\theta_0 = -13°$. With $\Delta\theta = 10°$, we are in the second case. For these values, we find relative amplitudes of 5%. This simple estimate is similar to the observed relative amplitude.

Figure 14 shows the relative intensity amplitude taken from the *TRACE* observation as a function of loop distance. This is

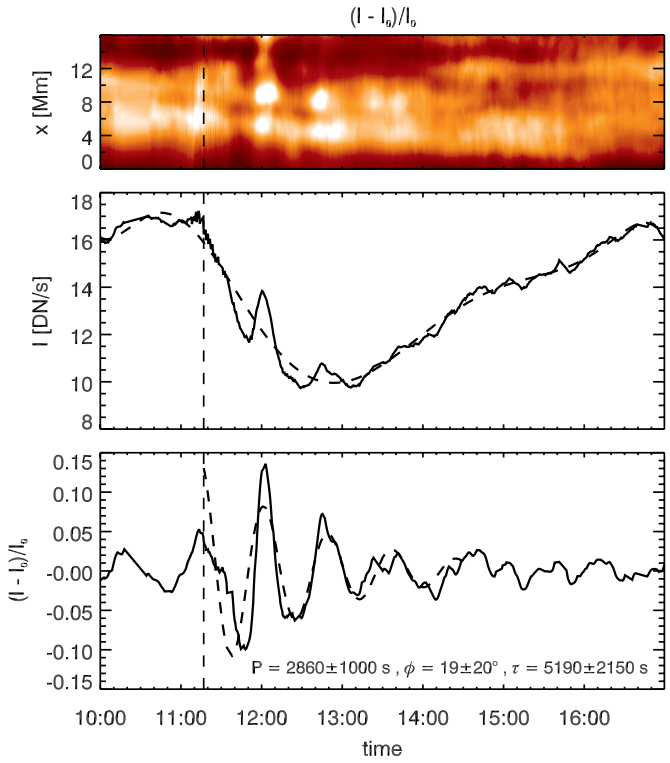

Figure 12. Top: relative intensity of the *TRACE* two-dimensional loop region, averaged over the longitudinal coordinate from the footpoint up to 22 Mm, as a function of time and transverse distance. The vertical dashed line indicates the reference time t_0. Middle: intensity of the same region, averaged over transverse distance, as a function of time. The dashed line is a smooth trend that is taken to be the background intensity. Bottom: relative intensity fitted with a damped oscillator between times t_0 and t_1 is shown as a dashed curve.

(A color version of this figure is available in the online journal.)

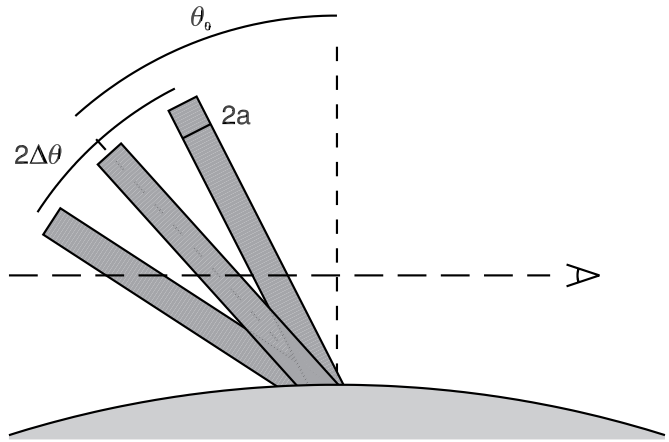

Figure 13. Principle of variations in line-of-sight integration due to a transverse loop oscillation in a loop of width $2a$ that is inclined by an angle θ_0. A simplified geometry is chosen where the line of sight is perpendicular to the photospheric normal and the loop baseline.

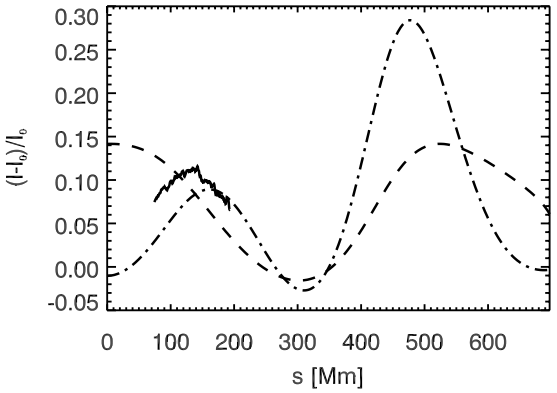

Figure 14. Relative intensity from *TRACE* as a function of loop distance with curves of relative intensity based on variations in line-of-sight column depth for the loop geometry with $\Delta\theta = -10^\circ$ and $f_3 = 0$ (dashed) and $f_3 = -0.37$ (dot-dashed).

compared with theoretical relative intensities based on variations in the line-of-sight column depth, calculated by taking into account the full loop geometry. We examine two cases with fixed perturbation inclination $\Delta\theta = -10^\circ$ and using Equation (2) with $f_3 = 0$ and $f_3 = -0.37$. The found relative intensities are of the same order as the *TRACE* observation, and therefore the variations in column depth may indeed explain the observation. Intensity variations are more difficult to extract from the EIT data. Therefore, it is not possible to extract the relative intensity profile along the whole loop.

It is debatable whether the loop inclination changes near the footpoint because of line-tying. However, if the footpoint intensity oscillations are to be explained by variations in line-of-sight column depth, then the loop inclination needs to vary at the footpoint. Possibly, for more complicated loop displacement profiles, the sign of the intensity variations may reverse, as suggested in Figure 14 with the case $f_3 = -0.37$.

6. CORONAL ALFVÉN SPEED PROFILE

The Alfvén speed obtained from the loop bundle no. 2 is 410 ± 40 km s^{-1}. This speed is the average Alfvén speed in the loop. It is about half the value of the typical speeds that have been deduced from previous studies for which the loop length is 3 times shorter. Since the magnetic field strength in a loop arcade is expected to decrease with loop length, it is conceivable that the Alfvén speed can be lower in a larger loop. However, it will also depend on the average loop density. We study the Alfvén speed across multiple loops in more detail.

The oscillations of a whole coronal arcade above an active region provide information of the Alfvén speed profile at different loops as a function of height in the global corona, which may be compared with magnetic field extrapolation models. With each oscillating loop, we can associate an average value of the average Alfvén speed (in that loop) and a loop length and height, or range of heights, in the corona. For instance, we can compare the observed Alfvén speeds with a height model of the Alfvén speed that includes gravitational and magnetic stratification:

$$V_A = V_{A0} \left(\frac{B}{B_0}\right) \left(\frac{\rho}{\rho_0}\right)^{1/2}, \quad (3)$$

where B_0 and ρ_0 are the magnetic field strength and density at a reference height z_0. The density profile is of the form

$$\rho = \rho_0 \exp\left[-\left(\frac{R_\odot^2}{H(R_\odot + z_0)}\right)\frac{z - z_0}{R_\odot + z}\right], \quad (4)$$

and the magnetic field strength is dipolar, i.e., $B = B_0(z/z_0)^{-3}$. For a given loop model with $z = (h + R\sin\phi)\cos\theta$ and where ϕ is the loop angle, the Alfvén speed profile is calculated and averaged over the loop. Thus, we find an Alfvén speed profile as a function of loop length, as shown in Figure 15. The

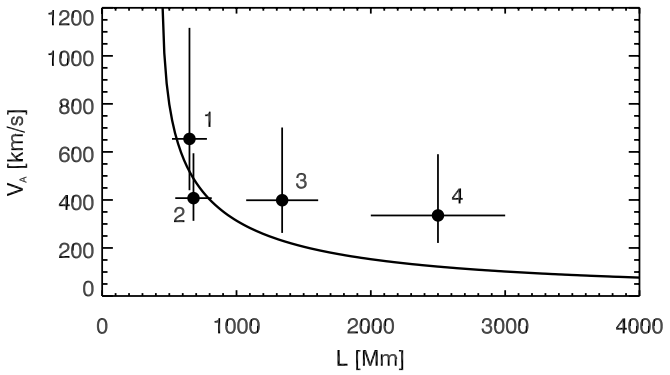

Figure 15. Alfvén speed profile as a function of loop length. The measured Alfvén speed from four loops is shown. The error bars take into account uncertainties in loop length, oscillation period, and loop density contrast.

profile underestimates the measured Alfvén speeds at larger distances. However, the measurements of loops 3 and 4 have large uncertainties and the modeling of the Alfvén speed profile here is quite basic. Modeling of active regions using nonlinear extrapolation shows that the resulting Alfvén speed profile can be flatter (e.g., Régnier et al. 2008). The result presented here is a first preliminary attempt to show the potential of using measurements of Alfvén speeds from transverse loop oscillations to model the global Alfvén speed profile and more work needs to be done.

7. CONCLUSIONS

We report the first observation of long-period transverse oscillations in large loops with periods in the range of 24–180 minutes. This demonstrates that the large-scale corona is oscillating in response to an eruption. The displacement amplitudes are of the order of 10 Mm. We have studied one loop bundle in detail and found an oscillation period and damping time of 40.3 minutes and 61 ± 5 minutes, respectively. The quality factor $\tau/P = 1.48 \pm 0.03$ is similar to what has been found for transverse loop oscillations with shorter periods of around 5 minutes and 3 times shorter loop lengths (Aschwanden et al. 2002). This result strongly indicates that the mechanism responsible for the observed damping is independent of loop length and period. For instance, this lends support to a mechanism based on resonant mode conversion (Goossens et al. 2002).

In addition, this study reveals the presence of an intensity oscillation associated with the transverse motions similar to those reported in Verwichte et al. (2009). This oscillation has a similar period to the transverse oscillation. Modeling shows that the intensity oscillation is most likely due to variations in the line-of-sight column depth. Such intensity variations provide an interesting new diagnostic channel as they contain information about the three-dimensional loop orientation. However, it remains unclear why the footpoints of the loops also show similar period intensity variations that are 180° out of phase with respect to the intensity oscillations in the loop itself.

We have for the first time measured the transverse displacement profile along the full length of the loop. To model this as a horizontally polarized mode, a planar loop geometry with an inclination corresponding to a minimum in loop curvature variations is perturbed by inclining the loop plane by a constant angular amplitude. This can reproduce the observed projected displacement profile. Smaller deviations can be explained by modifying the perturbation to include a third spatial longitudinal harmonic with an amplitude of −0.37 relative to the fundamental mode. Such modifications are expected when taking into account longitudinal stratification in models of kink modes in large loops. Thus, the perturbed loop is no longer planar. The value of the third harmonic amplitude departs much more from zero than theory predicts (Andries et al. 2009). However, in that study the theoretical values are determined under the assumption of small longitudinal structuring whilst here the loop radius is 2–3 times larger than the density scale height. Therefore, more elaborate (numerical) modeling (e.g., Verth et al. 2007) is required to describe the displacement profile in such circumstances. Also, the perturbation model used in terms of a constant inclination angular amplitude is simplistic and can be improved by using the kink eigenfunctions from curved loop models (Van Doorsselaere et al. 2004; Ruderman 2009; Van Doorsselaere et al. 2009c).

We have shown that the deviations may also be explained by a constant angle inclination perturbation of a non-planar equilibrium loop. The lack of sufficient detailed information of the full three-dimensional geometry makes ambiguous the direct modeling of the transverse displacement profile as a function of loop distance using spatial information from one kink harmonic. The method of using periods of multiple harmonics within the same loop seems superior in comparison to the technique of spatial seismology as it does not require at first order information of the three-dimensional loop geometry. However, observations of events with multiple periods are rare. Therefore, for the reliable application of spatial information in seismology, instruments such as the EUVI pairs, in combination with *TRACE* or the Atmospheric Imaging Array, are essential to help constrain the three-dimensional loop geometry. Together with the study reported by Verwichte et al. (2009), this study shows that instruments such as EUVI on board *STEREO* or the upcoming Atmospheric Imaging Array on board the Solar Dynamics Observatory can provide new opportunities on transverse oscillations of large loops and arcades.

E.V. acknowledges the financial support from the Engineering and Physical Sciences Research Council (EPSRC) Science and Innovation award. C.F. acknowledges financial support from the UK Science and Technology Facilities Council (STFC) on the CFSA Rolling Grant. T.V.D. acknowledges the support from the Marie Curie Intra European Fellowship within the 7th European Community Framework Programme under grant agreement no. 220555.

APPENDIX

We detail the method of determining a three-dimensional loop geometry from a set of N image coordinates outlining the projected loop, i.e., (X_i, Y_i). These coordinates are made relative to the solar disk center and in units of solar radii: $x_i = (X_i - X_c)/R_s$ and $y_i = (Y_i - Y_c)/R_s$. We can define the following useful vectors. First, the loop footpoints define the vectors $\boldsymbol{r}_{\rm I} = (x_{\rm I} = x_1, y_{\rm I} = y_1, z_{\rm I} = (1 - x_1^2 - y_1^2)^{1/2})$ and $\boldsymbol{r}_{\rm II} = (x_{\rm II} = x_N, y_{\rm II} = y_N, z_{\rm II} = (1 - x_N^2 - y_N^2)^{1/2})$. The baseline mid point is $\boldsymbol{r}_m = (\boldsymbol{r}_{\rm I} + \boldsymbol{r}_{\rm II})/2$. We can define a local coordinate system with the origin at $\boldsymbol{r}_m$ and unit vectors $\boldsymbol{e}_b = (\boldsymbol{r}_{\rm II} - \boldsymbol{r}_{\rm I})/|\boldsymbol{r}_{\rm II} - \boldsymbol{r}_{\rm I}|$, $\boldsymbol{e}_n = \boldsymbol{r}_m/r_m$ and $\boldsymbol{e}_t = \boldsymbol{e}_b \times \boldsymbol{e}_n$. A loop plane is defined by three points $\boldsymbol{r}_{\rm I}$, $\boldsymbol{r}_{\rm II}$, and $\boldsymbol{r}_{\rm III}(x_{\rm III}, y_{\rm III}, z_{\rm III}) = \boldsymbol{r}_m + \boldsymbol{e}_n + \boldsymbol{e}_t \tan\theta$, where θ is the inclination of the plane with respect to the photospheric normal.

A loop point with depth coordinate z_i lies within the plane if

$$\begin{vmatrix} x_i & y_i & z_i & 1 \\ x_{\rm I} & y_{\rm I} & z_{\rm I} & 1 \\ x_{\rm II} & y_{\rm II} & z_{\rm II} & 1 \\ x_{\rm III} & y_{\rm III} & z_{\rm III} & 1 \end{vmatrix} = 0, \tag{A1}$$

from which z_i is eliminated as

$$z_i = \frac{-\begin{vmatrix} y_{\rm I} & z_{\rm I} & 1 \\ y_{\rm II} & z_{\rm II} & 1 \\ y_{\rm III} & z_{\rm III} & 1 \end{vmatrix} x_i + \begin{vmatrix} x_{\rm I} & z_{\rm I} & 1 \\ x_{\rm II} & z_{\rm II} & 1 \\ x_{\rm III} & z_{\rm III} & 1 \end{vmatrix} y_i + \begin{vmatrix} x_{\rm I} & y_{\rm I} & z_{\rm I} \\ x_{\rm II} & y_{\rm II} & z_{\rm II} \\ x_{\rm III} & y_{\rm III} & z_{\rm III} \end{vmatrix}}{\begin{vmatrix} x_{\rm I} & y_{\rm I} & 1 \\ x_{\rm II} & y_{\rm II} & 1 \\ x_{\rm III} & y_{\rm III} & 1 \end{vmatrix}}. \tag{A2}$$

A simple model of a non-planar loop requires the loop points to lie on the surface of a cylinder whose axis is parallel to the loop baseline. This model involves two free parameters: inclination θ and cylinder radius ρ. The latter parameter is a measure of the non-planarity of the loop. In the limit of $\rho \rightarrow \infty$ a plane loop is recovered. The axis line is defined as $\boldsymbol{r}_a = \boldsymbol{r}_o + \lambda\, \boldsymbol{e}_b$, where $\boldsymbol{r}_o = \boldsymbol{r}_m + (\cos\theta\, \boldsymbol{e}_t - \sin\theta\, \boldsymbol{e}_n)\rho$ and λ is the line parameter. A loop point $\boldsymbol{r}_i$ lies on the cylinder surface if $|\boldsymbol{r}_i - \boldsymbol{r}_a| = \rho$ with $\lambda = (\boldsymbol{r}_i - \boldsymbol{r}_o).\boldsymbol{e}_b$. Thus, the condition becomes $|\boldsymbol{r}_i - \boldsymbol{r}_o - (\boldsymbol{r}_i - \boldsymbol{r}_o).\boldsymbol{e}_b\boldsymbol{e}_b| = \rho$ from which z_i is eliminated in terms of a quadratic $A\,(z_i - z_o)^2 - 2B\,(z_i - z_o) + C = 0$ with

$$\begin{aligned} A &= 1 - e_{bz}^2 \\ B &= [e_{bx}(x_i - x_o) + e_{by}(y_i - y_o)]\, e_{bz} \\ C &= [(x_i - x_o)^2 + (y_i - y_o)^2] \\ &\quad - [e_{bx}(x_i - x_o) + e_{by}(y_i - y_o)]^2 - \rho^2. \end{aligned} \tag{A3}$$

The solution with the loop point closest to $\boldsymbol{r}_m$ is

$$z_i = z_o + \frac{B - \mathrm{sgn}(B)\sqrt{B^2 - AC}}{A}. \tag{A4}$$

Because the cylinder has to be large enough to cover the loop point in the plane of the sky, there is a minimum value of ρ for which a solution can exist. It is given by $\rho^2 \geqslant [e_{bx}(y_i - y_o) - e_{by}(x_i - x_o)]/(e_{bx}^2 + e_{by}^2)$.

REFERENCES

Andries, J., Arregui, I., & Goossens, M. 2009, A&A, 497, 265
Andries, J., Goossens, M., Hollweg, J. V., Arregui, I., & Van Doorselaere, T. 2005, A&A, 430, 1109
Andries, J., Van Doorsselaere, T., Roberts, B., Verth, G., Verwichte, E., & Erdélyi, R. 2010, Space Sci. Rev., 149, 3
Arregui, I., Terradas, J., Oliver, R., & Ballester, J. L. 2008, ApJ, 674, 1179
Aschwanden, M. J. 2010, Space Sci. Rev., 149, 31
Aschwanden, M. J., De Pontieu, B., Schrijver, C. J., & Title, A. M. 2002, Sol. Phys., 206, 99
Aschwanden, M. J., Fletcher, L., Schrijver, C. J., & Alexander, D. 1999a, ApJ, 520, 880
Aschwanden, M. J., Newmark, J. S., Delaboudinière, J.-P., Neupert, W. M., Klimchuk, J. A., Gary, G. A., Portier-Fozzani, F., & Zucker, A. 1999b, ApJ, 515, 842
Brady, C. S., & Arber, T. D. 2005, A&A, 438, 733
Brady, C. S., Verwichte, E., & Arber, T. D. 2006, A&A, 449, 389
Cooper, F. C., Nakariakov, V. M., & Tsiklauri, D. 2003, A&A, 397, 765
Delaboudinière, J.-P., et al. 1995, Sol. Phys., 162, 291
De Moortel, I., & Brady, C. S. 2007, ApJ, 664, 1210
Edwin, P. M., & Roberts, B. 1983, Sol. Phys., 88, 179
Erdélyi, R., & Verth, G. 2007, A&A, 462, 743
Foullon, C., Verwichte, E., Nakariakov, V. M., & Fletcher, L. 2005, A&A, 440, L59
Goossens, M., Andries, J., & Aschwanden, M. J. 2002, A&A, 394, L39
Goossens, M., Terradas, J., Andries, J., Arregui, I., & Ballester, J. L. 2009, A&A, 503, 213
Handy, B. N., et al. 1999, Sol. Phys., 187, 229
Hori, K., Ichimoto, K., Sakurai, T., Sano, I., & Nishino, Y. 2005, ApJ, 618, 1001
Katsiyannis, A. C., Williams, D. R., McAteer, R. T. J., Gallagher, P. T., Keenan, F. P., & Murtagh, F. 2003, A&A, 406, 709
Luna, M., Terradas, J., Oliver, R., & Ballester, J. L. 2008, ApJ, 676, 717
Mikhalyaev, B. B., & Solov'ev, A. A. 2005, Sol. Phys., 227, 249
Morton, R. J., & Erdélyi, R. 2009, ApJ, 707, 750
Nakariakov, V. M., & Ofman, L. 2001, A&A, 372, L53
Nakariakov, V. M., Ofman, L., DeLuca, E. E., Roberts, B., & Davila, J. M. 1999, Science, 285, 862
Ofman, L., & Aschwanden, M. J. 2002, ApJ, 576, L153
O'Shea, E., Srivastava, A. K., Doyle, J. G., & Banerjee, D. 2007, A&A, 473, L13
Régnier, S., Priest, E. R., & Hood, A. W. 2008, A&A, 491, 297
Ruderman, M. S. 2009, A&A, 506, 885
Ruderman, M. S., & Roberts, B. 2002, ApJ, 577, 475
Terradas, J., & Ofman, L. 2004, ApJ, 610, 523
Terradas, J., Oliver, R., & Ballester, J. L. 2006, ApJ, 650, L91
Tomczyk, S., McIntosh, S. W., Keil, S. L., Judge, P. G., Schad, T., Seeley, D. H., & Edmondson, J. 2007, Science, 317, 1192
Van Doorsselaere, T., Birtill, D. C. C., & Evans, G. R. 2009, A&A, 508, 1485
Van Doorsselaere, T., Debosscher, A., Andries, J., & Poedts, S. 2004, A&A, 424, 1065
Van Doorsselaere, T., Nakariakov, V. M., & Verwichte, E. 2007, A&A, 473, 959
Van Doorsselaere, T., Nakariakov, V. M., & Verwichte, E. 2008a, ApJ, 676, L73
Van Doorsselaere, T., Nakariakov, V. M., Young, P. R., & Verwichte, E. 2008b, A&A, 487, 17
Van Doorsselaere, T., Verwichte, E., & Terradas, J. 2009c, Space Sci. Rev., 149, 299
Verth, G., & Erdélyi, R. 2008, A&A, 486, 1015
Verth, G., Van Doorsselaere, T., Erdélyi, R., & Goossens, M. 2007, A&A, 475, 341
Verwichte, E., Aschwanden, M. J., Van Doorsselaere, T., Foullon, C., & Nakariakov, V. M. 2009, ApJ, 698, 397
Verwichte, E., Foullon, C., & Nakariakov, V. M. 2006a, A&A, 449, 769
Verwichte, E., Foullon, C., & Nakariakov, V. M. 2006b, A&A, 452, 615
Verwichte, E., Nakariakov, V. M., & Cooper, F. C. 2005, A&A, 430, L65
Verwichte, E., Nakariakov, V. M., & Longbottom, A. 1999, J. Plasma Phys., 62, 219
Verwichte, E., Nakariakov, V. M., Ofman, L., & DeLuca, E. E. 2004, Sol. Phys., 223, 77
Wang, T. J., & Solanki, S. K. 2004, A&A, 421, L33
Wang, T. J., Solanki, S. K., & Selwa, M. 2008, A&A, 489, 1307